SCIEPublish

Article

Evaluation of the Effect of Fe_2O_3 as a Sintering Additive on Densification, Microstructure, and Thermal Stability of Al_2O_3

Pedro Henrique Poubel Mendonça da Silveira [1,*], Amal Elzubair Eltom [2], Naiara Vieira Le Sénéchal [1], Jheison Lopes dos Santos [3], Alaelson Vieira Gomes [1] and Marcelo Henrique Prado da Silva [1]

[1] Department of Materials Science, Military Institute of Engineering—IME, Praça General Tibúrcio 80, Urca, Rio de Janeiro 22290-270, Brazil; naiaravls@gmail.com (N.V.L.S.); alaelson@ime.eb.br (A.V.G.); marceloprado@ime.eb.br (M.H.P.d.S.)

[2] Materials Technology Group, Brazilian Navy Research Institute—IPqM, Rua Ipiru, 02, Cacuia, Rio de Janeiro 21931-095, Brazil; amal@ime.eb.br (A.E.E.)

[3] Brazilian Institute of Medicine and Rehabilitation, IBMR, Rio de Janeiro 22631-002, Brazil; jheisonls@hotmail.com (J.L.d.S.)

* Corresponding author. E-mail: pedroo.poubel@gmail.com (P.H.P.M.d.S.)

Received: 6 January 2025; Accepted: 20 March 2025; Available online: 26 March 2025

ABSTRACT: This study investigates the fabrication of alumina-based (Al_2O_3) ceramics using pressureless sintering, employing hematite (Fe_2O_3) as a sintering aid. Fe_2O_3 powders were synthesized via combustion and incorporated into Al_2O_3 concentrations of 0.5, 1.0, and 2.0 wt.%. The samples were sintered at 1400 °C and characterized by X-ray diffraction (XRD) with Rietveld refinement, thermogravimetric analysis (TG/DTG), scanning electron microscopy (SEM), energy-dispersive X-ray spectroscopy (EDX), and density measurements using the Archimedes method. The results demonstrated that the addition of Fe_2O_3 increased the densification of Al_2O_3 ceramics, with the highest densification (~85%) observed in samples containing 1.0 and 2.0 wt.% Fe_2O_3. XRD analysis identified only the corundum phase of Al_2O_3, suggesting that Fe_2O_3 was incorporated without forming secondary phases. However, Rietveld refinement calculations revealed distortions in the unit cell volume, which contributed to lowering the melting temperature of Al_2O_3, thereby facilitating sintering. SEM images showed that Fe_2O_3 acted as a grain growth inhibitor, resulting in finer microstructures with smaller grains. EDX mapping indicated that Fe ions preferentially accumulated in regions with higher pore concentrations. Thermal analysis demonstrated improved thermal stability in Fe_2O_3-containing samples. Overall, the study confirms that Fe_2O_3 serves as an effective sintering aid, enhancing densification and thermal stability while refining the microstructure of Al_2O_3 ceramics. These findings contribute to the development of optimized ceramic materials for high-performance applications.

Keywords: Al_2O_3; Fe_2O_3; Sintering aid; Microstructure; XRD; TGA

1. Introduction

Alumina-based ceramics (Al_2O_3) have been extensively studied and applied in various industrial sectors due to their exceptional properties, making them strategic materials for a wide range of applications. Al_2O_3 is widely used in structural components, cutting tools, high-performance coatings, and biomedical devices, such as prostheses and dental implants. Its extensive use is attributed to remarkable properties, including high thermal stability, wear resistance, dimensional integrity, and exceptional hardness—factors that ensure superior performance under extreme conditions such as high temperatures, intense friction, and exposure to aggressive chemical agents [1,2]. However, despite these advantages, ceramics in general exhibit significant limitations due to their brittle nature, making them susceptible to crack propagation and catastrophic failures under high stresses. Low flexural strength and limited fracture toughness present challenges for the development of these ceramics in applications requiring greater impact resistance and abrupt load variations. Consequently, recent research has focused on developing strategies to enhance the toughening of ceramics, whether through the introductionn of reinforcing phases, microstructural modifications, or advanced manufacturing processes [3,4].

To improve the properties of Al_2O_3, sintering additives are employed, allowing the modification of the conventional solid-state sintering (SSS) process to liquid-phase sintering (LPS). This method, widely used in the production of advanced ceramics, enables the achievement of dense and homogeneous structures. LPS occurs when low-melting-point additives are incorporated into the base material, forming a liquid phase during heating [5]. This liquid phase "wets" the ceramic particles, promoting their rearrangement, increasing atomic diffusion rates, and facilitating particle coalescence at lower temperatures, resulting in greater material densification. Sintering additives are extensively used in the fabrication of advanced ceramics, such as metallic oxides and carbides, whose high melting points require techniques that enable efficient sintering [6]. Among the most commonly used additives for liquid-phase formation are metallic oxides such as CaO, MgO, BaO, Nb_2O_5, Y_2O_3, SiO_2, and ZrO_2, which lower the sintering temperature and improve the final microstructure. Additionally, ternary eutectic compositions are employed to generate liquid phases with low melting points, with the choice of these compositions depending on the desired ceramic properties [7–27]. However, precise control of the liquid phase's quantity and composition is essential, as an excess can lead to phase segregation or excessive grain growth, compromising the material's mechanical strength [6]. Controlled cooling after sintering also influences the distribution of the solidified liquid phase, affecting the final product's porosity and thermal stability. In technological applications, this process is widely used in the fabrication of electronic components, wear-resistant coatings, and high-performance cutting materials, where the combination of high hardness and good fracture toughness is essential [28,29].

In the case of Al_2O_3, efficient sintering can be achieved by introducing hematite (Fe_2O_3) as an additive. The Al_2O_3-Fe_2O_3 system is a widely studied mixed oxide compound with applications in catalysis and adsorption. This material has been the subject of various investigations due to its physicochemical properties [30–34]. Al_2O_3 is notable for its high mechanical strength, thermal stability, surface acidity, and insulating properties, while Fe_2O_3 is known for its redox behavior, sintering ease, and semiconductor and antiferromagnetic properties [35,36].

The use of Fe_2O_3 as a sintering additive in Al_2O_3 contributes to the improvement of its mechanical properties. In terms of application, this system can be utilized in the fabrication of oxidation catalysts with enhanced thermal stability, as well as powders with high mechanical resistance and improved redox functionality [37]. The study of the Al_2O_3-Fe_2O_3 compound began in the 20th century with pioneering work by Muan [37] and Muan and Gee [38], in which a phase diagram of this system was developed to better understand the formation of its crystalline phases. Building on this initial study, various researchers have expanded the knowledge of this material, allowing a better understanding of the phases and microstructure resulting from the interaction between the two oxides [39–42].

Based on studies of the Al_2O_3-Fe_2O_3 system and aiming to understand the mechanical properties of ceramics in this compound, we recently published a paper [4] investigating the influence of Fe_2O_3 on the mechanical properties of Al_2O_3. Concentrations ranging from 0 to 8 wt.% of Fe_2O_3 were analyzed, evaluating properties through dilatometry, density, flexural, and compression tests. The results indicated that additions of up to 2 wt.% of Fe_2O_3 improved the mechanical properties of Al_2O_3, whereas higher concentrations led to significant deterioration due to additive agglomeration during mixing, resulting from its high density.

2. Materials and Methods

2.1. Materials

The following materials were used in the production of ceramic bodies: α-Al_2O_3 (ρ = 3.96 g/cm^3; Alcoa P-913, Belém, Brazil), with a particle size of 1 μm, as well as glycine (Sigma Aldrich, Duque de Caxias, Brazil) and iron nitrate (Neon Química, Suzano, Brazil), which were employed in the synthesis of hematite (Fe_2O_3) powder (ρ = 5.26 g/cm^3). Polyethylene glycol (Isofar, Duque de Caxias, Brazil) was added to enhance the mechanical strength of the green bodies.

The theoretical density of the samples was determined using the Rule of Mixtures, as expressed in Equation (1). The calculation considered the densities and mass fractions of the composite components, excluding polyethylene glycol, since it is removed during the sintering process [43]. Table 1 presents the density values and the nomenclature adopted for each sample.

$$\rho = (\rho_a \cdot m_a) + (\rho_b \cdot m_b) \quad (1)$$

where ρ_{Al2O3} is the density of Al_2O_3, m_{Al2O3} is the weight fraction of Al_2O_3, ρ_{Fe2O3} is the density of Fe_2O_3, and m_{Fe2O3} is the weight fraction of Fe_2O_3. The compositions used in this study were based on the work of Silveira et al. [4], in which variations of 0, 0.5, 1, and 2 wt.% of Fe_2O_3 were employed.

Table 1. Nomenclature, composition, and theoretical density of the samples obtained by the rule of mixtures. Theoretical density values obtained from the compositions with permission from Ref. [4].

Sample	Composition	Density (g/cm^3)
AL	100 wt.% Al_2O_3	3.960
ALFE05	99.5 wt.% Al_2O_3—0.5 wt.% Fe_2O_3	3.966
ALFE10	99 wt.% Al_2O_3—1 wt.% Fe_2O_3	3.973
ALFE20	98 wt.% Al_2O_3—2 wt.% Fe_2O_3	3.986

2.2. Synthesis of Fe_2O_3 Powders

The preparation of Fe_2O_3 powders was carried out using the solution combustion synthesis method, as described by Cao et al. [44]. In this method, ferric nitrate [$Fe(NO_3)_3 \cdot 9H_2O$] was used as the oxidizing agent and glycine [NH_2CH_2COOH] as the fuel. To begin the process, $Fe(NO_3)_3 \cdot 9H_2O$ and glycine were dissolved in 150 mL of deionized (DI) water, and the solution was stirred until homogeneous. The mixture was then transferred to a 500 mL beaker and heated to 100 °C on a heating plate. During the heating, the water evaporated, and the mixture turned into a gelatinous mass, a process that lasted about 10 min. After this period, the mixture swelled, releasing gases, and the gel underwent a non-explosive exothermic reaction, resulting in spontaneous combustion. The final product of this process was a foam composed of iron oxide.

2.3. Ceramic Processing

The Al_2O_3, Fe_2O_3, and polyethylene glycol were initially homogenized in a ball mill for 8 h, using distilled water in a 1:1 ratio with the mixture to facilitate homogenization. After this, the powders were dried for 48 h. Once dried, the powders were manually deagglomerated and sieved through a 60 mesh sieve. Discs with a diameter of 15 mm and a mass of 0.5 g were formed by cold uniaxial pressing using a load of 30 MPa. Pressureless sintering was performed in a JUNG furnace, with the process reaching a maximum temperature of 1400 °C, followed by inertial cooling of the furnace. The sintering process path is shown in Figure 1.

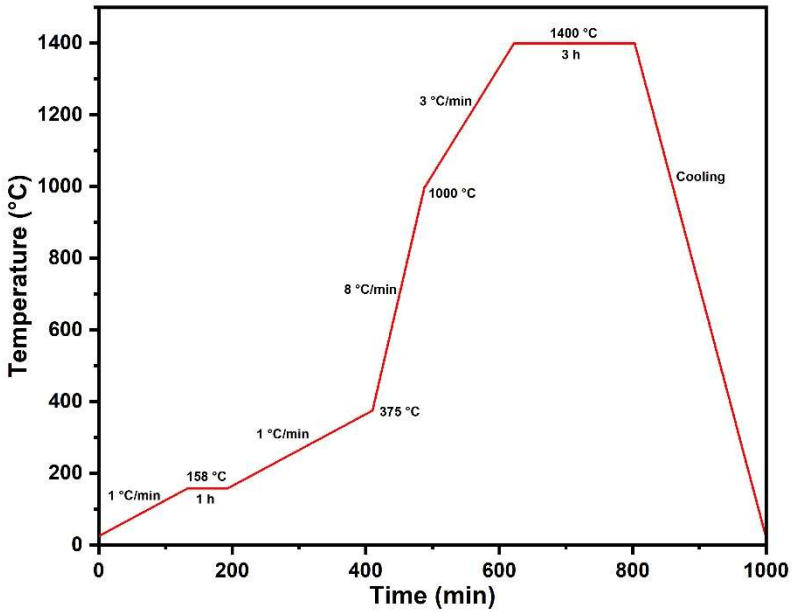

Figure 1. Heating ramp used for sintering of Al_2O_3-Fe_2O_3 ceramics. Reprinted with permission from Ref. [4].

2.4. Characterization

2.4.1. Density Measurement

From the theoretical density value found by the Rule of Mixtures, it was possible to calculate the density and densification of the green bodies. To find the density value of the green body, the mass difference by the volume of the sample was used. The relative density of the green bodies (d_{GB}), Equation (2), was calculated on the percentage difference of the density value (ρ_{green}) obtained by theoretical density (ρ_{td}) found in the Rule of Mixtures as:

$$d_{\mathrm{GB}} = \frac{\rho_{\mathrm{green}}}{\rho_{\mathrm{td}}} \times 100\% \quad (2)$$

The bulk density measurements were conducted on the sintered samples using Archimedes' principle, on an analytical balance with an attached density kit. The bulk density of the samples (ρ) was obtained by:

$$\rho = \frac{M_{dry}}{M_{dry} - M_{wet}} \times \rho_{liquid}\% \quad (3)$$

where, M_{dry} and M_{wet} are the masses of the sintered samples in air and liquid, respectively, and liquid is the density of water at room temperature. The linear shrinkage of the samples (L_s) was obtained by:

$$L_S = \frac{d_g - d_s}{d_s} \times 100\% \quad (4)$$

where d_g is the diameter of the green body and d_s is the diameter of the sintered body.

2.4.2. X-ray Diffraction (XRD)

The phase composition, crystallite size, and lattice parameter of the sintered samples were analyzed using XRD (X'Pert Pro MRD, Malvern Panalytical, São Paulo, Brazil) using Co Ka radiation generated at 40 kV and 25 mA. The crystallite size and lattice parameters of the samples were calculated from the XRD pattern and Rietveld refinement using the Debye–Scherrer's approximation:

$$D = \frac{k\lambda}{\beta \cdot cos\theta} \quad (5)$$

where D is the crystallite size (nm), λ is the wavelength of Co Ka radiation (λ = 1.7908 A), β is the full width at half maximum (FWHM) for the diffraction peak under consideration, θ is the diffraction angle, and k is the broadening constant.

2.4.3. Thermogravimetric Analysis (TG/DTG)

The TG/DTG and DTA analyses of the ceramic powders were performed in a Shimadzu DTG-60H machine (Shimadzu, Tokyo, Japan). The samples were carefully hand-crushed with a pestle/mortar and then were placed in a platinum crucible. The procedure was performed under a nitrogen atmosphere with a heating rate of 10 °C/min, from 20 to 900 °C.

2.4.4. Scanning Electron Microscopy (SEM) and Energy Dispersive Spectroscopy (EDX)

The morphology and elemental composition of the sintered samples were observed using SEM-FEG (Quanta 250 FEG, FEI, Hillsboro, OR, USA) operated at an accelerating voltage of 20 kV equipped with an EDX detector. The samples for SEM-FEG examination were prepared by placing the powders on a conductive carbon tape and further sputter coated with gold. The grain size was calculated using ImageJ software to count 100 grain size measurements, and OriginPro software was used to plot the histogram with the grain size distribution.

2.4.5. Statistical Analysis

The relative density results were subjected to statistical analysis through Analysis of Variance (ANOVA) to assess whether significant differences existed among the mean values, considering a 95% confidence level. ANOVA is a statistical method used to determine if the variations observed between group means are larger than what would be expected due to random sampling error alone. For performing the analysis of variance, OriginPro 2021 software was used. Following the ANOVA, pairwise comparisons of the means were performed using Tukey's HSD (Honestly Significant Difference) test, which is specifically designed to control the Type I error rate when making multiple comparisons. Tukey's test was applied to identify which specific pairs of means significantly differ from each other. The calculations for Tukey's HSD test are as follows [45]:

$$HSD = q\sqrt{\frac{EMS}{r}} \quad (6)$$

3. Results and Discussion

3.1. Effect of Fe_2O_3 on Densification

Table 2 presents the average results for density, relative densification of the green bodies and sintered samples, and linear shrinkage. The densification data, which were previously reported in [4] for compositions up to 2 wt.%, were included here to provide a comprehensive comparison and build upon the earlier findings, with a more detailed statistical analysis conducted in the present study.

Table 2. Values of density, densification and linear shrinkage of samples before and after sintering. Data obtained with permission from Ref. [4].

Sample	Density of Green Bodies (g/cm^3)	Relative Density of Green Bodies (%)	Density of Sintered Samples (g/cm^3)	Relative Density of Sintered Samples (%)	Linear Shrinkage (%)
AL	2.29 ± 0.09	57.79 ± 2.40	3.13 ± 0.11	78.88 ± 2.88	11.43 ± 0.43
ALFE05	2.41 ± 0.08	60.89 ± 1.91	3.13 ± 0.07	79.06 ± 1.89	13.55 ± 1.31
ALFE10	2.43 ± 0.10	61.13 ± 2.53	3.32 ± 0.03	83.61 ± 0.77	16.33 ± 0.36
ALFE20	2.35 ± 0.05	58.99 ± 1.36	3.41 ± 0.05	85.49 ± 1.38	16.16 ± 0.40

Based on the data presented in Table 2, it is clear that the inclusion of Fe_2O_3 affected the relative densification of the green bodies. Specifically, the additions of 0.5 and 1.0 wt.% resulted in an increase in the densification of the ALFE05 and ALFE10 samples, compared to the pure alumina sample (AL). On the other hand, the addition of 2.0 wt.% of Fe_2O_3 caused a slight reduction in the densification of the green bodies, with this group achieving 58.99% of the theoretical density.

For ceramics to achieve high densification after the sintering process, it is essential to consider the particle size distribution. According to Francis [46], unlike metallic powders, ceramic particles are difficult to deform, which hinder the compaction and formation of green bodies. As a result, green bodies typically reach between 50% and 60% of the theoretical density; in some cases, they can reach up to 65%. Due to their high strength and hardness, ceramic particles prevent effective compaction of the green body. In contrast, metallic powders can achieve much higher densification of green bodies since these materials have lower strength and deform easily under compaction pressure. Suresh et al. [47] observed this discrepancy in relative density between metallic and ceramic green bodies, presenting a relationship that involves the compaction of different metallic powders. Considering the variation in the metal and the applied compaction pressure, achieving up to 90% of the theoretical density in metallic powders is possible. ANOVA statistical analysis was performed to verify whether the values obtained for green densification were statistically similar, taking into account the high standard deviation found for each group. The results found are presented in Table 3.

Table 3. Variance Analysis for the green density of analyzed samples.

Causes of Variation	Degrees of Freedom	Sum of Squares	Mean Square	F (Calculated)	F (Critical)
Treatment	3	45.77	15.26	3.44	3.10
Residue	20	88.61	4.43		
Total	23	134.38			

From the ANOVA calculations, it is possible to affirm that the results obtained for the groups studied are statistically different, considering that $F_{calculated} > F_{critical}$. In order to determine which values differ from each other, Tukey's test was performed with a value of HSD = 3.40. Through Equation (6), the results obtained by the Tukey test are shown in Table 4.

Table 4. HSD (honestly significant difference) test for the green density of analyzed samples.

Sample	AL	ALFE05	ALFE10	ALFE20
AL	0.00	3.10	3.35	1.21
ALFE05	3.10	0.00	0.25	1.89
ALFE10	3.35	0.25	0.00	2.14
ALFE20	1.21	1.89	2.14	0.00

The results shown in Table 4 indicated that the values are statistically equal for all but the groups because all values of the mean difference between the groups are lower than the HSD value.

The addition of Fe_2O_3 to Al_2O_3 caused an increase in the relative densification of the sintered samples. The addition of 0.5 wt.% of Fe_2O_3 resulted in an average densification of 78.88%, however, its standard deviation was high, resulting

in samples with different densifications. With increasing Fe_2O_3 content, an increase in densification occurred, coupled with a reduction in standard deviation. The ALFE10 and ALFE20 groups presented average densifications of 83.61 and 85.49% for sintering at 1400 °C, respectively. The values achieved were higher than those found in the work of Gomes et al. [48] for the sintering of pure Al_2O_3 (AL) at temperatures of 1400 and 1600 °C, where the authors obtained average densification of 71.8% for sintering at 1600 °C. This comparison shows that the addition of Fe_2O_3 caused a considerable increase in the densification of the pure AL sample.

The linear shrinkage results followed the same trend as the increase in relative densification. As the densification of the samples increased, the linear shrinkage also increased, however, the ALFE20 sample suffered a small reduction in the linear shrinkage value. The same statistical calculation was performed for the densification of the sintered samples. The ANOVA results are shown in Table 5.

Table 5. Analysis of variance for the densification of sintered samples.

Causes of Variation	Degrees of Freedom	Sum of Squares	Mean Square	F (Calculated)	F (Critical)
Treatment	3	197.51	65.83	18.27	3.10
Residue	20	72.07	3.60		
Total	23	269.58			

From the ANOVA calculations, it is possible to affirm that the results obtained for the groups studied are statistically different, considering that $F_{calculated} > F_{critical}$. In order to know which values, differ from each other, Tukey's test was performed with a value of HSD = 3.07. The results obtained by the Tukey test are shown in Table 6.

Table 6. HSD (honestly significant difference) test for the densification of the sintered samples.

Sample	AL	ALFE05	ALFE10	ALFE20
AL	0.00	0.17	4.73	6.61
ALFE05	0.17	0.00	4.55	6.43
ALFE10	4.73	4.55	0.00	1.88
ALFE20	6.61	6.43	1.88	0.00

The results presented in Table 6 indicated the statistical difference from the AL and ALFE05 groups to the ALFE10 and ALFE20 groups, due to the difference in densification groups obtained by adding 1 and 2 wt.% of Fe_2O_3. Between AL and ALFE05 there is no statistical difference, due to the fact that the difference was smaller than the HSD value. The same occurred upon comparing ALFE10 and ALFE20 groups.

3.2. Effect of Fe_2O_3 on Phase

The precursor powders used in this work (Al_2O_3 and Fe_2O_3) were analyzed by XRD to identify the phases present in Figure 2.

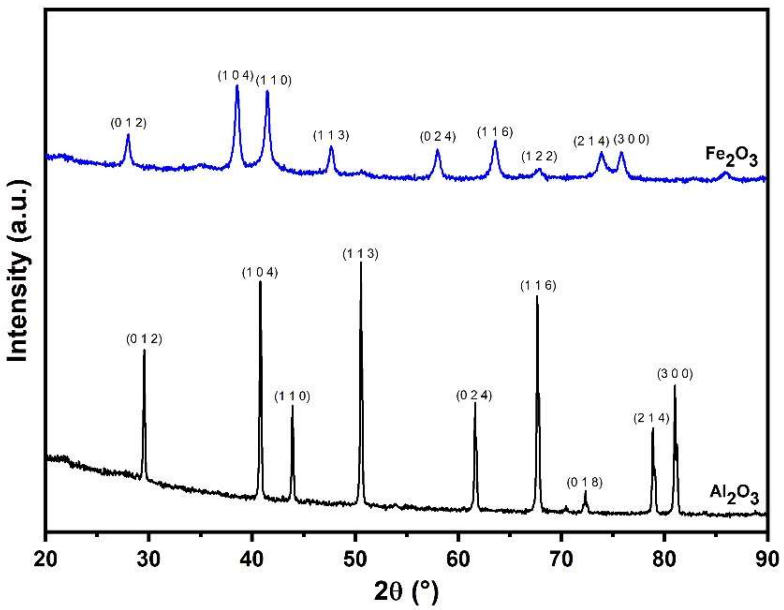

Figure 2. XRD patterns of Al_2O_3 and Fe_2O_3 powders.

The diffractogram of Al_2O_3 shows the presence of α-Al_2O_3 of rhombohedral structure, identified by crystallographic file JCPDS 00-005-0712 (Corundum). The crystallographic planes of Al_2O_3 shown in the corresponding peaks refer to the crystallographic planes of this structure. The Al_2O_3 normally occurs with the hexagonal structure. However, during Al_2O_3 production, the high calcination temperatures, above 750 °C transform the structure from hexagonal to rhombohedral, regardless of the use of precursors and/or additives [49].

The JCPDS crystallographic file JCPDS 00-033-0664 (Burnt Ochre) referring to hematite (α-Fe_2O_3) identifies the Fe_2O_3 powder with a rhombohedral crystal structure. The α-Fe_2O_3 has octahedral coordination, where the Fe atom is bonded to six oxygen atoms, causing the structure to become rhombohedral, similar to the corundum found in α-Al_2O_3 [50]. This is evidenced in the diffractograms of Al_2O_3 and Fe_2O_3, where the peaks of the two materials indicate the same crystallographic planes. Therefore, they showed the same crystal structure, except for the (1 2 2) plane, which appears at 67.72° in the diffractogram of Fe_2O_3 and does not appear in the diffractogram of Al_2O_3.

Figure 3 shows the Rietveld refined diffractograms of the sintered samples. From the Rietveld refinement performed on the XRD patterns, only the α-Al_2O_3 phase was found, refined by space group R-3c of the rhombohedral structure of corundum. No phases related to Fe_2O_3 or $AlFeO_3$ were found, indicating only corundum formation. According to the phase diagram of Al_2O_3-Fe_2O_3 system in which, only corundum formation will occur with the addition of hematite up to 12 wt.%. As no hematite-related peaks were found during the analysis, this is attributed to its formation below 5%, which is the detection limit of the X-ray diffractometer [51].

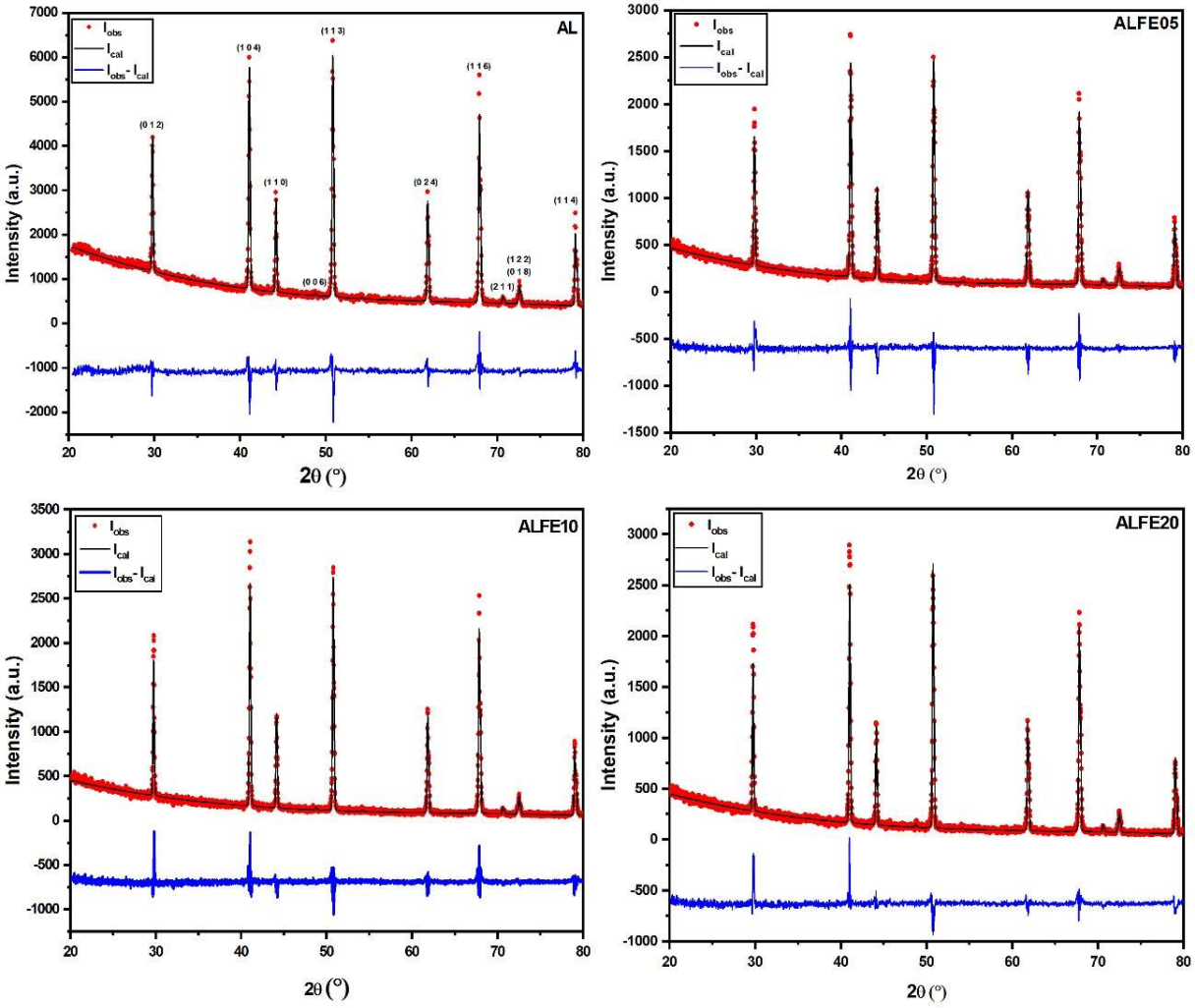

Figure 3. Rietveld refinement plot of sintered samples.

The formation of $AlFeO_3$, occurs by the homogenization of Al_2O_3 with Fe_2O_3, followed by diffusion during sintering. Indeed, the substitution of Fe^{3+} ions for Al^{3+} ions occurs to form an orthorhombic structure [52,53]. ABO_3-ordered materials, called perovskite, are known to exhibit photocatalytic and photoluminescent properties [54]. Despite few studies about the formation of $AlFeO_3$, some works report the emergence of this phase through the synthesis of Al_2O_3 doped with Fe or Fe_2O_3. In all works, an increase in catalytic activity from the presence of $AlFeO_3$ was reported

[55,56]. Thus, the formation of $AlFeO_3$, even if not detected by XRD, may have a direct relationship with the increase in the densification of the samples when compared with the densification of pure Al_2O_3, processed with similar parameters in the works of Gomes et al. [48] and Lopes et al. [17].

Based on the data presented in Table 7, several trends can be observed regarding the crystallite size, lattice parameters, and unit cell volume of the sintered samples. The crystallite size of the pure alumina sample (AL) was found to be 65.001 nm, which serves as a baseline for comparison. Upon adding 0.5 wt.% of Fe_2O_3, the crystallite size decreased to 56.690 nm, indicating that the incorporation of small amounts of Fe_2O_3 inhibited the growth of crystallites. This reduction may be attributed to the increased nucleation sites provided by the Fe_2O_3, which likely promoted a finer grain structure. However, further additions of Fe_2O_3, specifically 1.0 and 2.0 wt.%, led to an increase in crystallite size. The samples ALFE10 and ALFE20 exhibited crystallite sizes of 69.862 nm and 66.990 nm, respectively. This increase could result from a more pronounced sintering process, where larger crystallites form due to the coalescence of smaller particles or enhanced diffusion at higher Fe_2O_3 concentrations. This trend reflects the complex interplay between nucleation and growth that occurs during the sintering process.

Table 7. Lattice parameters of sintered samples.

Sample	D (nm)	DP (nm)	a = b (nm)	c (nm)	V (nm^3)
AL	65.001	5.440	4.759	12.995	254.955
ALFE05	56.690	4.554	4.761	13.001	255.295
ALFE10	69.862	6.013	4.762	13.002	255.360
ALFE20	66.990	5.672	4.763	13.004	255.525

In addition to the crystallite size, the samples' lattice parameters (a, b, and c) slightly increased with higher Fe_2O_3 content. Specifically, the values of the unit cell parameters for the AL sample were a = 4.759 nm, b = 4.759 nm, and c = 12.995 nm. For the ALFE05, ALFE10, and ALFE20 samples, the parameters showed a small but consistent increase in both the a, b, and c values, with the largest increase in the c parameter. This suggests that the Fe_2O_3 incorporation led to slight changes in the crystal structure, likely due to the substitution of Al^{3+} ions by Fe^{3+} ions or interstitial occupation by oxygen atoms, which can cause slight lattice distortions.

Consequently, the unit cell volume also increased with the addition of Fe_2O_3. The unit cell volume for the AL sample was 254.955 nm^3, and this value increased slightly with the incorporation of Fe_2O_3, reaching 255.295 nm^3 for the ALFE05 sample, 255.360 nm^3 for the ALFE10 sample, and 255.525 nm^3 for the ALFE20 sample. These increases in unit cell volume reflect the cumulative effect of changes in lattice spacing and the incorporation of heavier Fe^{3+} ions into the crystal lattice, which can expand the unit cell slightly.

3.3. Morphological Analysis

The surface morphology of the sintered samples was investigated using SEM (Scanning Electron Microscopy), and the images are presented in Figure 4. The grain size of the sintered samples was also evaluated to verify the influence of Fe_2O_3 on the grain growth of Al_2O_3, with a histogram showing the grain size distribution. SEM images provide direct information about the morphology of the samples.

The image of the AL sample exhibits a large number of pores due to low densification during sintering; however, the average grain size was the largest among all the sintered samples. The AL group presented D = 2.79 ± 0.96 μm, resulting from disordered grain growth and the possible occurrence of the Ostwald ripening phenomenon during sintering, in which larger particles grow at the expense of smaller particles, "engulfing" them. This phenomenon can occur when there is a disparity in particle size. In contrast to disordered grain growth, the absence of additives in this sample led to a high presence of pores. Particle size also directly affects the densification of Al_2O_3 during sintering since smaller particles result in materials with higher surface energy, which allows for higher densification and, consequently, greater mechanical strength [57].

The addition of 0.5 wt.% of Fe_2O_3 promoted a slight increase in the densification of the ALFE05 group samples. A lower number of pores was observed; however, the grain growth of Al_2O_3 was considerably reduced, generating grains with irregular sizes. The average grain size of the sintered ALFE05 sample was D = 1.20 ± 0.67 μm. Due to the increase in densification, a slight growth in the grain size of the ALFE10 and ALFE20 groups occurred, which can be observed in the corresponding micrographs, showing more densified surfaces and the presence of isolated, spherical-shaped pores, indicating that the material entered the final stage of sintering [6].

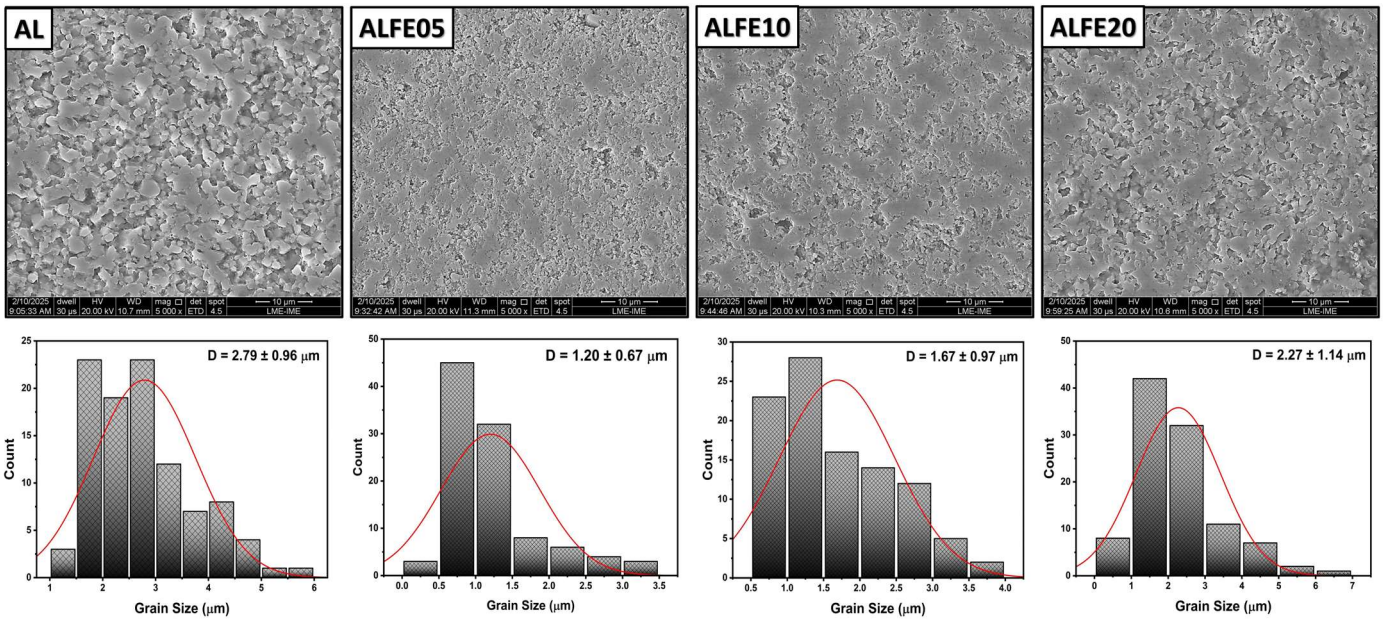

Figure 4. Micrographs of the surface of Al_2O_3-Fe_2O_3 ceramics and their respective grain size distribution histograms after sintering.

The addition of Fe_2O_3 in contents of 1 and 2 wt.% resulted in larger grain sizes, with ALFE10 and ALFE20 samples obtaining values of D = 1.67 ± 0.97 μm and 2.27 ± 1.14 μm, respectively. The isolation of pores is also highlighted in the ALFE20 group. This sample, which showed the highest densification among the four studied groups, exhibited the largest grain growth. However, the average grain size was still smaller than that of pure Al_2O_3 (AL). This may be associated with the action of Fe_2O_3 in inhibiting Al_2O_3 grain growth, exhibiting a behavior similar to that of MgO [58].

Figure 5 and Table 8 show the EDX spectra with the compositional map of the sintered samples and the quantification of each present element, respectively. In the AL sample analysis, aluminum and oxygen atoms are observed, as expected for the sample without a sintering additive. On the other hand, the ALFE05, ALFE10, and ALFE20 samples show the presence of iron, highlighted in blue.

As observed, with the increase in Fe_2O_3 content, the Fe concentration also appeared higher in the spectrum, being distributed throughout the sample. However, the compositional map of the ALFE20 sample indicates Fe concentration in regions with a higher number of pores or larger grains. This predominance of Fe in the pores can be explained by the fact that Fe_2O_3 is denser than Al_2O_3, leading to small agglomeration regions. Additionally, the high surface energy of Fe_2O_3 powders, obtained through the self-combustion technique, may have contributed to the formation of these agglomerations at higher Fe_2O_3 contents.

Table 8. Elemental composition (wt.%) of the elements found in the EDX map.

Sample	Al (wt.%)	O (wt.%)	Fe (wt.%)
AL	67.70	32.30	-
ALFE05	67.19	32.01	0.80
ALFE10	67.32	31.42	1.27
ALFE20	66.91	30.94	2.55

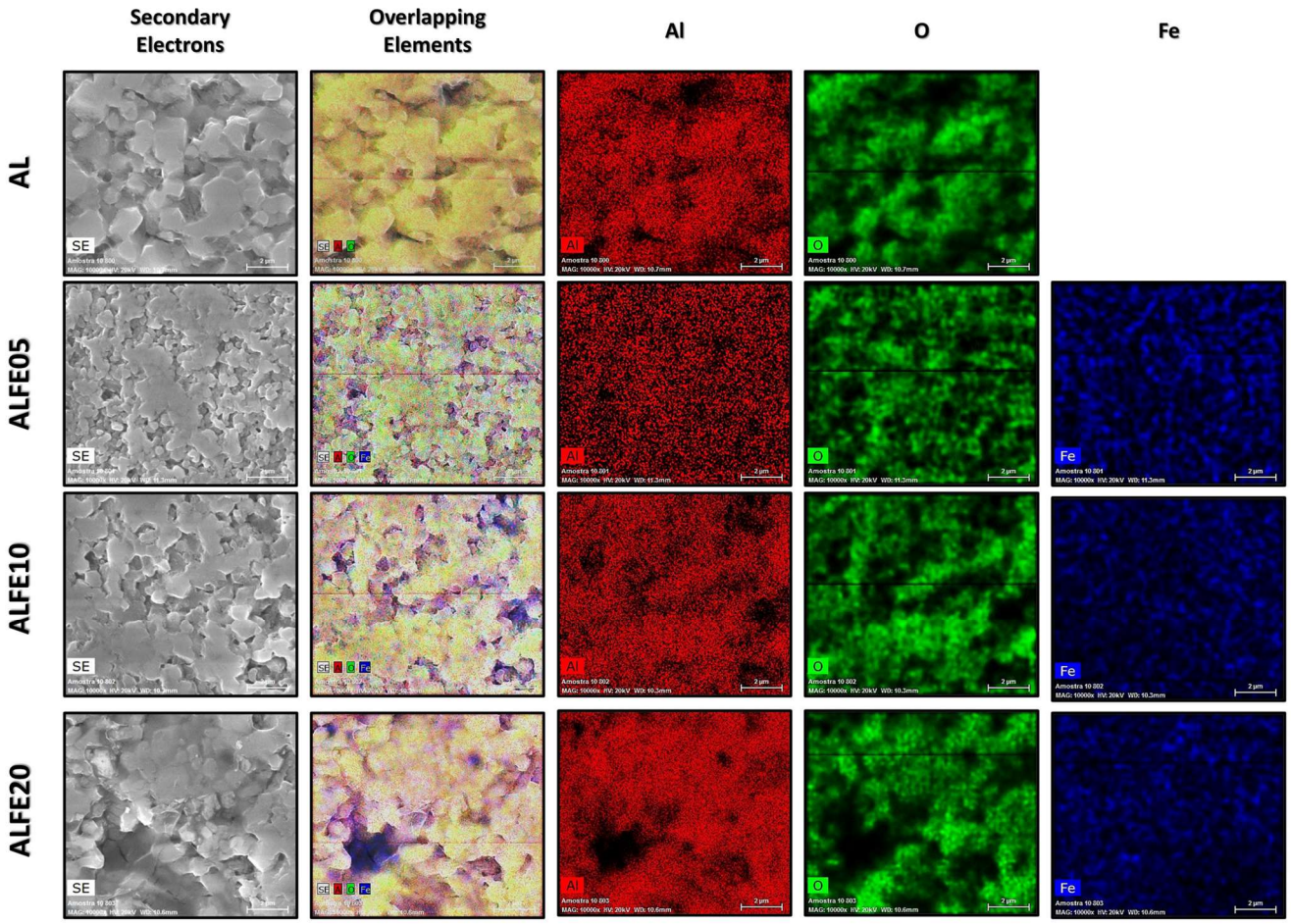

Figure 5. Compositional map of sintered Al_2O_3-Fe_2O_3 samples.

3.4. Thermal Analysis

Figure 6 shows the TG/DTG curves of samples ALFE05, ALFE10 and ALFE20.

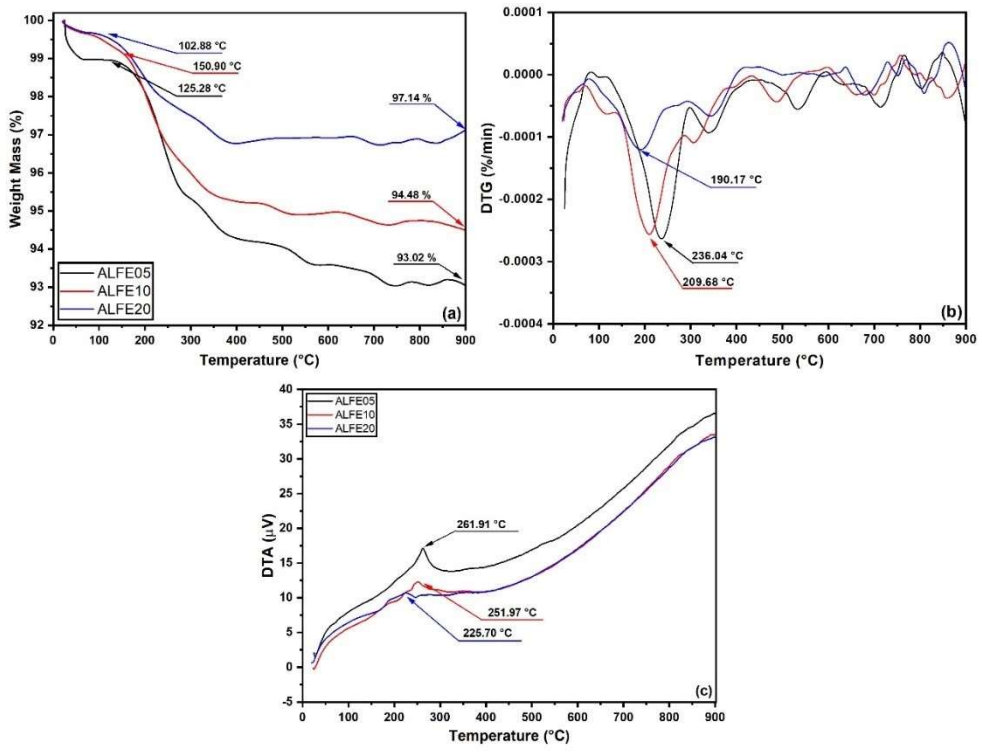

Figure 6. Thermal analysis plots of ALFE05, ALFE10 and ALFE20 samples: (**a**) TG; (**b**) DTG; (**c**) DTA.

The addition of Fe_2O_3 influences the onset of degradation. The sample ALFE05 showed the beginning of the degradation event, resulting from the elimination of the polyethylene glycol (PEG) at 125.28 °C. The maximum degradation point was defined from the DTG plot in Figure 6b, where the peak of thermal degradation is shown at 236.04 °C. The PEG degradation event in sample ALFE05 ended at the T_{endset} temperature, which was 287.65 °C. At the end of the test, at 900 °C, the material showed a residue percentage of 93.02%. The addition of Fe_2O_3 in higher contents resulted in a change in the TG curve of the ALFE10 and ALFE20 samples. The sample with 1 wt.% Fe_2O_3 showed T_{onset} at higher temperature (150.90 °C). The peak of the DTG curve indicates that the maximum degradation occurred at 209.68 °C, and T_{endset} occurred at 261.83 °C. The sample with 2 wt.% Fe_2O_3 showed anticipation in the thermal events when compared to the other two samples, in which T_{onset} = 102.88 °C, T_{max} = 190.17 °C, and T_{endset} = 243.17 °C. The addition of the sintering aid in higher contents promoted an increase in thermal stability, where the residue at 900 °C of the ALFE10 and ALFE20 samples was 94.48 and 97.14%, respectively.

4. Conclusions

In this paper, the effect of hematite (Fe_2O_3) as a sintering additive in alumina (Al_2O_3) ceramics and its influence on densification, phase formation, microstructure, and thermal stability were investigated. The results of this study demonstrated that the addition of Fe_2O_3 as a sintering aid positively influenced the densification, thermal stability, and microstructure of the produced ceramics. The samples with 1 and 2 wt.% Fe_2O_3 exhibited densification close to 85%, higher than that of pure alumina, indicating that hematite promotes pore filling and increases the final density of the material. X-ray diffraction analysis did not identify the formation of secondary phases, such as $AlFeO_3$, suggesting that, at the concentrations used, Fe_2O_3 does not significantly alter the crystalline structure of Al_2O_3, remaining in the corundum form. However, Rietveld analysis revealed small variations in lattice parameters, unit cell volume, and crystallite size, indicating that Fe_2O_3 caused a distortion in the Al_2O_3 lattice, breaking some covalent bonds and enabling effective sintering of Al_2O_3 at 1400 °C. SEM images showed a more densified microstructure, with smaller grains and a homogeneous distribution, which contributes to more balanced mechanical properties. Additionally, Fe_2O_3 exhibited behavior similar to MgO, acting as an inhibitor of uncontrolled grain growth, favoring the production of a material with better microstructural control. The elemental mapping by EDX indicated that iron ions concentrated in more porous regions, which may be related to the higher density of Fe_2O_3 and its high surface energy. Thermal analysis revealed that increasing the Fe_2O_3 content improved the thermal stability of the samples, reducing thermal degradation and increasing the final residue at high temperatures.

Based on these results, sintered Al_2O_3-Fe_2O_3 ceramics have great potential for advanced applications. One of the main possibilities is their use in ballistic protection, as the increased densification and thermal stability enhance impact resistance and energy dissipation in high-velocity impacts. Additionally, these ceramics can be applied in the production of refractory materials for high-temperature environments, such as industrial furnaces and boiler linings, where thermal stability and wear resistance are essential. Another relevant application is in catalysts and catalytic supports, taking advantage of the chemical interaction between Al_2O_3 and Fe_2O_3 to improve the efficiency of heterogeneous reactions. Furthermore, these ceramics can be employed in high-performance structural components in the aerospace and automotive industries due to their mechanical strength and chemical stability. Thus, the combination of these properties significantly expands the application range of Al_2O_3-Fe_2O_3 ceramics, making them promising materials for various technological and industrial sectors.

Acknowledgments

The authors thank the Brazilian agencies CNPq, CAPES, and FAPERJ for supporting this investigation. This study was financed in part by the Coordenação de Aperfeiçoamento de Pessoal de Nível Superior—Brasil (CAPES)—Finance Code 001. The authors thank the Brazilian Navy Research Institute (IPqM) researchers for performing the thermal analyses. Pedro Henrique Poubel Mendonça da Silveira and Marcelo Henrique Prado da Silva thank the Fundação de Amparo à Pesquisa do Estado do Rio de Janeiro (FAPERJ) for their support—grant numbers E-26/200.338/2024 and 200.339/2024.

Author Contributions

Conceptualization, P.H.P.M.d.S. and A.V.G.; Methodology, P.H.P.M.d.S. and A.V.G.; Software, P.H.P.M.d.S.; A.E.E.; J.L.d.S.; Validation, M.H.P.d.S. and A.V.G.; Formal Analysis, P.H.P.M.d.S.; Investigation, P.H.P.M.d.S. and N.V.L.S.; Resources, M.H.P.d.S.; Data Curation, A.E.E.; Writing—Original Draft Preparation, P.H.P.M.d.S. and

N.V.L.S.; Writing—Review & Editing, J.L.d.S.; Visualization, A.V.G. and M.H.P.d.S.; Supervision, M.H.P.d.S.; Project Administration, M.H.P.d.S.; Funding Acquisition, A.V.G.

Ethics Statement

Not applicable.

Informed Consent Statement

Not applicable.

Data Availability Statement

The data supporting findings of this study are available upon reasonable request.

Funding

This research was funded by the Carlos Chagas Filho Foundation for Research Support of the State of Rio de Janeiro (FAPERJ), grant numbers E-26/200.338/2024 and E-26/200.339/2024.

Declaration of Competing Interest

The authors declare that they have no known competing financial interests or personal relationships that could have appeared to influence the work reported in this paper.

References

1. Baltazar J, Alves MFRP, dos Santos C, Olhero S. Reactive sintering of Al_2O_3–$Y_3Al_5O_{12}$ ceramic composites obtained by direct ink writing. *Ceramics* **2022**, *5*, 1–12.
2. Prathumwan R, Subannajui K. Fabrication of a ceramic/metal (Al_2O_3/Al) composite by 3D printing as an advanced refractory with enhanced electrical conductivity. *RSC Adv.* **2020**, *10*, 32301–32308.
3. Silveira P, Silva T, Ribeiro M, Rodrigues de Jesus P, Credmann P, Gomes A. A brief review of alumina, silicon carbide and boron carbide ceramic materials for ballistic applications. *Acad. Lett.* **2021**, *1*, 1–11.
4. Silveira PHPM, Eltom AE, Santos JL, Delaqua GCG, Vieira CMF, Jesus PRR, et al. Addition of hematite as a sintering aid in alumina: Effect of concentration on physical, microstructural and mechanical properties. *Tecnol. EmMetal. Mater. Mineração* **2024**, *21*, 2978.
5. Keramat E, Hashemi B. Modelling and optimizing the liquid phase sintering of alumina/CaO–SiO_2–Al_2O_3 ceramics using response surface methodology. *Ceram. Int.* **2021**, *47*, 3159–3172.
6. German RM, Suri P, Park SJ. Liquid phase sintering. *J. Mater. Sci.* **2009**, *44*, 1–39.
7. Zawrah M, Shaw L. Liquid-phase sintering of SiC in presence of CaO. *Ceram. Int.* **2004**, *30*, 721–725.
8. Yin D, Wang J, Ni M, Liu P, Dong Z, Tang D. Fabrication of highly transparent Y_2O_3 ceramics with CaO as sintering aid. *Materials* **2021**, *14*, 444.
9. Lee JW, Cha JM, Bae BH, Choi SW, Jung HD, Yoon CB. Effects of using MgO, CaO additives as sintering aid in pressureless sintering of $M_2Si_5N_8$: Eu^{2+} (M= Ba, Sr) phosphor ceramics for amber LED automotive applications. *J. Alloys Compd.* **2021**, *858*, 157710.
10. Souto P, Menezes R, Kiminami R. Sintering of commercial mulite powder: Effect of MgO dopant. *J. Mater. Process. Technol.* **2009**, *209*, 548–553.
11. Sutorik AC, Gilde G, Cooper C, Wright J, Hilton C. The effect of varied amounts of LiF sintering aid on the transparency of alumina rich spinel ceramic with the composition $MgO{\cdot}1.5Al_2O_3$. *J. Am. Ceram. Soc.* **2012**, *95*, 1807–1810. doi:10.1111/j.1551-2916.2012.05197.x.
12. Fabris DCN, Polla MB, Acordi J, Luza AL, Bernardin AM, De Noni A, Jr. Effect of $MgO{\cdot}Al_2O_3{\cdot}SiO_2$ glass-ceramic as sintering aid on properties of alumina armors. *Mater. Sci. Eng. A* **2020**, *781*, 139237. doi:10.1016/j.msea.2020.139237.
13. Li T, Segawa H, Ohashi N. Sintering behavior and dielectric properties of $BaTiO_3$ added with BaO-Bi_2O_3-B_2O_3 glass phase. *Ceram. Int.* **2018**, *44*, 13004–13010. doi:10.1016/j.ceramint.2018.03.113.
14. Meng Q, Zhao Z, Sun Y, Li X, Ji H. Low temperature pressureless sintering of dense silicon nitride using BaO-Al_2O_3-SiO_2 glass as sintering aid. *Ceram. Int.* **2017**, *43*, 10123–10129. doi:10.1016/j.ceramint.2017.05.219.
15. Pan C, Zhao G, Li S, Wang J, Yin L, Song W, et al. Effect of BaO-$2B_2O_3$ sintering aid on the structural and electrical properties of $CaBi_2Nb_2O_9$ high-temperature piezoelectric ceramic. *J. Appl. Phys.* **2021**, *130*, 244102. doi:10.1063/5.0071675.

16. Da Silveira PHP, De Jesus PRR, Ribeiro MP, Monteiro SN, De Oliveira JCS, Gomes AV. Sintering behavior of Al_2O_3 ceramics doped with pre-sintered Nb_2O_5 and LiF. *Mater. Sci. Forum* **2020**, *1012*, 190–195. doi:10.4028/www.scientific.net/MSF.1012.190.
17. Dos Santos JL, Marçal RLSB, De Jesus PRR, Gomes AV, Lima ÉP, Jr., Da Rocha DN, et al. Mechanical properties and ballistic behavior of LiF-added Al_2O_3–4 wt% Nb_2O_5 ceramics. *J. Mater. Res. Technol.* **2018**, *7*, 592–597. doi:10.1016/j.jmrt.2018.06.013.
18. Silveira PHP, Eltom AE, Gomes AV, Silva MHPD. Sintering behavior, phase formation, physical and mechanical properties of Al_2O_3—Nb_2O_5 ceramics produced by pressureless sintering using Fe_2O_3 as sintering aid. *Mater. Lett.* **2024**, *359*, 135966. doi:10.1016/j.matlet.2024.135966.
19. Gomez E, Echeberria J, Iturriza I, Castro F. Liquid phase sintering of SiC with additions of Y_2O_3, Al_2O_3 and SiO_2. *J. Eur. Ceram. Soc.* **2004**, *24*, 2895–2903. doi:10.1016/j.jeurceramsoc.2003.10.041.
20. Shan K, Li R, Liu J. Effect of Y_2O_3 on the corrosion resistance of two-step sintered $Al_5Y_3O_{12}$-$MgAl_2O_4$ sidewalls in the aluminum electrolyte. *J. Eur. Ceram. Soc.* **2022**, *42*, 1815–1821. doi:10.1016/j.jeurceramsoc.2021.11.010.
21. Wang L, Wang S, Xing P, Yang M, Li H, Zhuang Y, et al. High-performance B4C-YB4 composites fabricated with Y_2O_3 additive via hot-pressing sintering. *Ceram. Int.* **2022**, *48*, 26269–26277. doi:10.1016/j.ceramint.2022.02.090.
22. De Carvalho ANC, De Sousa Melo JJ, Sales FHS. Medidas elétricas e dielétricas em cerâmicas de $BaTiO_3$ dopadas com SiO_2 e Bi_2O_3. *Braz. J. Dev.* **2022**, *8*, 6871–6899. doi:10.34117/bjdv8n1-153.
23. Gomes AV, Lima É, Jr., De Jesus PRR, Nascimento LFC, Dos Santos JL, Monteiro SN, et al. Novel alumina compounds with niobia, silica and magnesia for ballistic armor. *Mater. Sci. Forum* **2020**, *1012*, 196–201. doi:10.4028/www.scientific.net/MSF.1012.196.
24. Qin X, Wu H, Chen C, Ao H, Li W, Gao R, et al. Enhanced energy-storage performance of $Pb_{0.925}La_{0.05}Zr_{0.95}Ti_{0.05}$@ xwt% SiO_2 composite ceramics. *J. Alloys Compd.* **2022**, *890*, 161869. doi:10.1016/j.jallcom.2021.161869.
25. Corado HP, Silveira PH, Ortega VL, Ramos GG, Elias CN. Flexural strength of vitreous ceramics based on lithium disilicate and lithium silicate reinforced with zirconia for CAD/CAM. *Int. J. Biomater.* **2022**, *2022*, 5896511. doi:10.1155/2022/1234567.
26. Yi Q, Zhou S, Teng H, Lin H, Hou X, Jia T. Structural and optical properties of Tm transparent ceramic with La_2O_3, ZrO_2 as composite sintering aid. *J. Eur. Ceram. Soc.* **2012**, *32*, 381–388. doi:10.1016/j.jeurceramsoc.2011.09.003.
27. Zaki ZI, Alotaibi SH, Alhejji BA, Mostafa NY, Amin MA, Qhatani MM. Combustion synthesis of high density ZrN/$ZrSi_2$ composite: Influence of ZrO_2 addition on the microstructure and mechanical properties. *Materials* **2022**, *15*, 1698.
28. Svancarek P, Galusek D, Ghillanyova K, Sedláček J, Kozánková J, Šajgalík P. The influence of additives on microstructure of sub-micron alumina ceramics prepared by two-stage sintering. *J. Eur. Ceram. Soc.* **2012**, *32*, 1965–1970. doi:10.1016/j.jeurceramsoc.2012.02.002.
29. Sktani ZDI, Rejab NA, Ratnam MM, Ahmad ZA. Fabrication of tougher ZTA ceramics with sustainable high hardness through (RSM) optimisation. *Int. J. Refract. Met. Hard Mater.* **2018**, *74*, 78–86. doi:10.1016/j.ijrmhm.2018.03.013.
30. Hu J, Li H, Chen S, Xiang W. Enhanced Fe_2O_3/Al_2O_3 oxygen carriers for chemical looping steam reforming of methane with different Mg ratios. *Ind. Eng. Chem. Res.* **2022**, *61*, 1022–1031. doi:10.1021/acs.iecr.1c04359.
31. Jiang Y, Mao Q, Ma T, Liu X, Li Y, Ren S. Facile preparation of Fe_2O_3/Al_2O_3 composite with excellent adsorption properties towards Congo red. *Ceram. Int.* **2021**, *47*, 13884–13894. doi:10.1016/j.ceramint.2021.02.124.
32. Liu L, Zachariah MR. Enhanced performance of alkali metal doped Fe_2O_3 and Fe_2O_3/Al_2O_3 composites as oxygen carrier material in chemical looping combustion. *Energy Fuels* **2013**, *27*, 4977–4983. doi:10.1021/ef400683q.
33. Yan P, Zhang K, Peng Y. Study of Fe_2O_3-Al_2O_3 catalyst reduction parameters and conditions for catalytic methane decomposition. *Chem. Eng. Sci.* **2022**, *250,* 117410. doi:10.1016/j.ces.2022.117410.
34. Ma Z, Liu G, Lu Y, Zhang H. Redox performance of Fe_2O_3/Al_2O_3 oxygen carrier calcined at different temperature in chemical looping process. *Fuel* **2022**, *310*, 122381. doi:10.1016/j.fuel.2021.122381.
35. Abyzov A. Aluminum oxide and alumina ceramics (review). Part 1. Properties of Al_2O_3 and commercial production of dispersed Al_2O_3. *Refract. Ind. Ceram.* **2019**, *60*, 24–32. doi:10.1007/s11148-019-00314-2.
36. Bercoff P, Bertorello H. Magnetic properties of hematite with large coercivity. *Appl. Phys. A* **2010**, *100*, 1019–1027. doi:10.1007/s00339-010-5857-1.
37. Muan A. On the stability of the phase $Fe_2O_3 \cdot Al_2O_3$. *Am. J. Sci.* **1958**, *256*, 413–422. doi:10.2475/ajs.256.5.413.
38. Muan A, Gee C. Phase equilibrium studies in the system iron oxide-Al_2O_3 in air and at 1 atm O_2 pressure. *J. Am. Ceram. Soc.* **1956**, *39*, 207–214. doi:10.1111/j.1151-2916.1956.tb15573.x.
39. Dayal R, Gard J, Glasser F. Crystal data on $FeAlO_3$. *Acta Crystallogr.* **1965**, *18*, 574–575. doi:10.1107/S0365110X65001388.
40. Feenstra A, Sämann S, Wunder B. An experimental study of Fe–Al solubility in the system corundum–hematite up to 40 kbar and 1300 °C. *J. Petrol.* **2005**, *46*, 1881–1892. doi:10.1093/petrology/egi044.
41. Dreval L, Zienert T, Fabrichnaya O. Calculated phase diagrams and thermodynamic properties of the Al_2O_3–Fe_2O_3–FeO system. *J. Alloys Compd.* **2016**, *657*, 192–214.

42. Majzlan J, Navrotsky A, Evans B. Thermodynamics and crystal chemistry of the hematite–corundum solid solution and the $FeAlO_3$ phase. *Phys. Chem. Miner.* **2002**, *29*, 515–526.
43. Kim HS. On the rule of mixtures for the hardness of particle reinforced composites. *Mater. Sci. Eng. A* **2000**, *289*, 30–33.
44. Cao Z, Qin M, Jia B, Gu Y, Chen P, Volinsky AA, et al. One pot solution combustion synthesis of highly mesoporous hematite for photocatalysis. *Ceram. Int.* **2015**, *41*, 2806–2812.
45. Nanda A, Mohapatra BB, Mahapatra A, Mahapatra AAPK. Multiple comparison test by Tukey's honestly significant difference (HSD): Do the confident level control type I error. *Int. J. Stat. Appl. Math.* **2021**, *6*, 59–65.
46. Francis LF. *Materials Processing: A Unified Approach to Processing of Metals, Ceramics, and Polymers*, 1st ed.; Academic Press: New York, NY, USA, 2015.
47. Suresh K, Mahendran S, Krupashankara M, Avinash L. Influence of powder composition & morphology on Green density for powder metallurgy processes. *Int. J. Innov. Res. Sci. Eng. Technol.* **2015**, *4*, 18629–18634.
48. Gomes A, Louro L, Costa C. Ballistic behavior of alumina with niobia additions. *J. Phys. IV* **2006**, *134*, 1009–1014.
49. Kim HS, Kang M. Rapid crystal phase transformation into hexagonally shaped α-alumina using AlF_3 seeds. *J. Sol-Gel Sci. Technol.* **2013**, *68*, 110–120.
50. Muhajir M, Puspitasari P, Razak JA. Synthesis and applications of Hematite α-Fe_2O_3: A review. *J. Mech. Eng. Sci. Technol.* **2020**, *3*, 51–58.
51. Hu P, Jiang Z, Liu Q, Heslop D, Roberts AP, Torrent J, et al. Estimating the concentration of aluminum-substituted hematite and goethite using diffuse reflectance spectrometry and rock magnetism: Feasibility and limitations. *J. Geophys. Res. Solid. Earth* **2016**, *121*, 4180–4194.
52. Li Q, Wang S, Yuan Y, Gao H, Xiang X. Phase-controlled synthesis, surface morphology, and photocatalytic activity of the perovskite $AlFeO_3$. *J. Sol-Gel Sci. Technol.* **2017**, *82*, 500–508.
53. Shireen A, Saha R, Mandal P, Sundaresan A, Rao C. Multiferroic and magnetodielectric properties of the $Al_{1-x}G_xFeO_3$ family of oxides. *J. Mater. Chem.* **2011**, *21*, 57–59.
54. Snytnikov V, Stoyanovskii V, Larina T, Krivoruchko O, Ushakov V, Parmon V. Laser-induced luminescence of model Fe/Al_2O_3 and Cr/Al_2O_3 catalysts. *Kinet. Catal.* **2008**, *49*, 291–298.
55. Lucio-Ortiz CJ, La Rosa D, Rivera J, Ramirez AH, De Los Reyes Heredia JA, Del Angel P, et al. Synthesis and characterization of Fe doped mesoporous Al_2O_3 by sol–gel method and its use in trichloroethylene combustion. *J. Sol-Gel Sci. Technol.* **2011**, *58*, 374–384.
56. Maldonado CS, La Rosa D, Rivera J, Lucio-Ortiz CJ, Hernández-Ramírez A, Barraza FFC, et al. Low concentration Fe-doped alumina catalysts using sol-gel and impregnation methods: The synthesis, characterization and catalytic performance during the combustion of trichloroethylene. *Materials* **2014**, *7*, 2062–2086.
57. Akhter R. Evaluation of mechanical properties of sintered nano alumina ceramic powder with different doping concentration. *Int. J. Eng. Technol. Res.* **2015**, *3*, 2454–4698.
58. Galusek D, Ghillanyova K, Sedláček J, Kozánková J, Šajgalík P. The influence of additives on microstructure of sub-micron alumina ceramics prepared by two-stage sintering. *J. Eur. Ceram. Soc.* **2012**, *32*, 1965–1970.